Fabrication of Large Area Metal-on-Carbon Catalytic Condensers for Programmable Catalysis

Kyung-Ryul Oh[1,2], Tzia Ming Onn[1,2], Amber Walton[2],
Michael L. Odlyzko,[3] C. Daniel Frisbie[1,2], Paul J. Dauenhauer[1,2,*]

[1] Center for Programmable Energy Catalysis (CPEC), University of Minnesota, 421 Washington Ave. SE,
  Minneapolis, MN, USA 55455
[2] University of Minnesota, Department of Chemical Engineering & Materials Science, 421 Washington Ave. SE,
  Minneapolis, MN, USA 55455
[3] University of Minnesota, Characterization Facility, 100 Union St. SE, Minneapolis, MN, 55455
* Corresponding author: hauer@umn.edu

Abstract. Catalytic condensers stabilize charge on either side of a high-k dielectric film to modulate the electronic states of a catalytic layer for electronic control of surface reactions. Here, carbon sputtering provided for fast, large-scale fabrication of metal-carbon catalytic condensers required for industrial application. Carbon films were sputtered on HfO_2 dielectric/p-type Si with different thickness (1, 3, 6, 10 nm), and the enhancement of conductance and capacitance of carbon films was observed upon increasing carbon thickness following thermal treatment at 400 °C. After Pt deposition on the carbon films, the Pt catalytic condenser exhibited high capacitance of ~210 nF/cm^2 that was maintained at a frequency ~1,000 Hz, satisfying the requirement for a dynamic catalyst to implement catalytic resonance. Temperature programmed desorption of carbon monoxide yielded CO desorption peaks which shifted in temperature with varying potential applied to the condenser (−6 V or 6 +V) indicating a shift in the binding energy of carbon monoxide on the Pt condenser surface. A substantial increase of capacitance (~2,000 nF/cm^2) of the Pt-on-carbon devices was observed at elevated temperatures of 400 °C that can modulate ~10% of charge per metal atom when 10 V potential was applied. A large catalytic condenser of 42 cm^2 area Pt/C/HfO$_2$/Si exhibited high capacitance of 9,393 nF with low leakage current/capacitive current ratio (<0.1), demonstrating the practicality and versatility of the facile, large-scale fabrication method for metal-carbon catalytic condensers.

Introduction. Catalytic cycles on surfaces comprised of a sequence of elementary steps including adsorption, surface reaction, and desorption have historically been optimized by identifying catalytic materials that provide the best overall rate, independent of the fastest conditions for each elementary reaction step. This approach has identified optimal materials consistent with the Sabatier principle, whereby the fastest catalysts exhibit moderate characteristics in relevant reaction descriptors such as adsorbed species binding energy.[1] Yet catalysts at the Sabatier maximum remain too slow for many important energy applications including ammonia synthesis, methanol synthesis, and hydrogen generation via electrolysis.[2-3]

Programmable catalysts overcome the limited rate and selectivity of catalytic reactions by modulating the electronic states of the active site on the time scale of the catalytic cycle. Oscillating a heterogeneous catalyst between two or more states leads to resonance conditions at select frequencies, whereby the catalyst switches once per catalytic cycle to conditions favorable for each rate-controlling elementary reaction.[4-5] This effect also controls the extent of reaction pathways for selectivity control and applies over a range of dynamic conditions.[6-7] The mechanisms enabling active site dynamics and catalytic resonance include the application of light, charge, and physical strain, all of which can potentially modulate the binding energy of surface species in excess of 20 kJ mol^{-1} at frequencies above 100 Hz.[8-11] These methods apply energy directly to the surface without changing overall (fluid-phase) reaction thermodynamics.[12]

Catalytic condensers have emerged as a platform device to implement programmable catalysis via the application of charge (electrons or holes) to the active site.[13] As a stack device comprised of multiple layers, the catalytic condenser uses a high-k dielectric film to separate
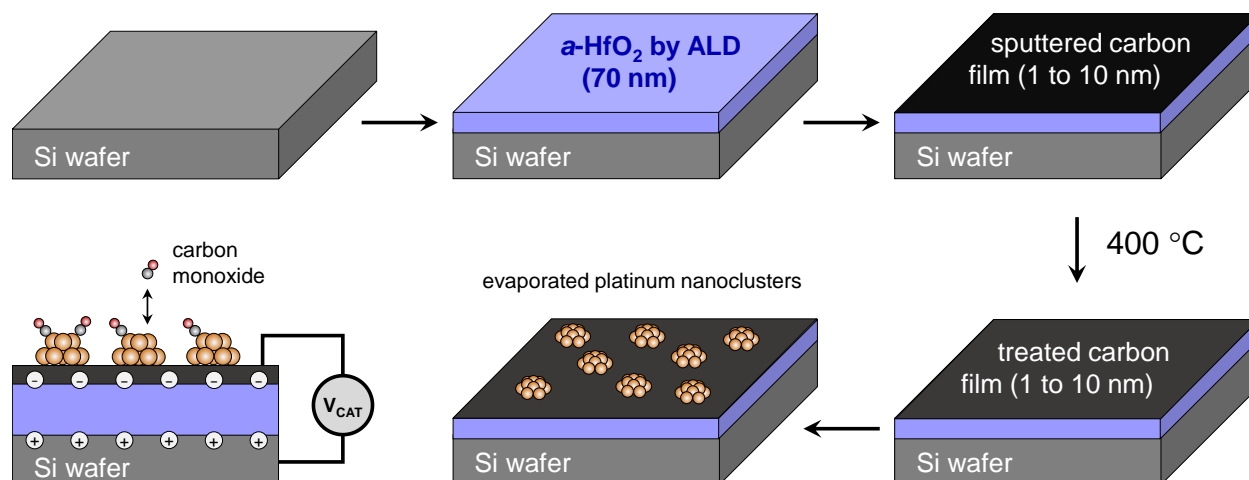
Scheme 1. Multi-step fabrication of platinum-on-carbon catalytic condensers by sequential atomic layer deposition (ALD), carbon sputtering, thermal treatment, and evaporation of metal to form nanoclusters.

two conductive films; the exposed top catalytic film is sufficiently thin to permit stabilized charge to influence the electronic properties of the active site. Catalytic condensers have been fabricated with 70 nm HfO_2 films capable of stabilizing capacitance as high as 980 nF cm^{-2} when heated to 240 °C.[14] The top catalytic layer consists of a sheet of graphene to conduct charge laterally across the device; catalytic thin films or particles are then deposited on top of the graphene. A catalytic condenser capable of removing electron density from ~4 nm amorphous alumina on graphene was shown to modulate the kinetics of alcohol dehydration by lowering the activation energy by 16 kJ mol^{-1}.[13] Similarly, a catalytic condenser comprised of ~4 nm Pt nanoclusters on graphene was shown to modulate the binding energy of carbon monoxide on Pt by about 20 kJ mol^{-1}.[14] These prototype devices ~1.0 cm^2 in size demonstrate the capability of electronically tunable catalytic surfaces by taking advantage of the high conductance and minimal capacitance of graphene layer, allowing for charge transfer over large distances that primarily resides in the catalytic material (not the graphene).

The prototype graphene-based catalytic condensers[13-14] exhibit significant capability for controlling the active sites for surface catalysis, yet scaling these devices to larger sizes for industrial application is limited by the cost and composition of their components, especially the graphene layer. Graphene transfer techniques are slow and complicated procedures with low reproducibility for obtaining high quality of the transferred graphene due to the cracks and wrinkles.[15] Direct

growth of monolayer or multilayer graphene on a substrate by chemical vapor deposition of reactive gases have been reported even for wafer-scale,[16-20] but these methods require high temperatures (650–1400 °C) as well as a specific type of substrate such as Cu,[21] Ni,[22] H-Ge,[23] and sapphire[24] for graphene growth.

Alternatively, thin amorphous carbon films have been grown for applications including diffusion barriers, hardmasks, electrodes, batteries, etc.[25-27] While graphene consists of sp^2 carbons with high conductivity and zero band gap and diamond consists of sp^3 carbons with low conductivity and a large band gap (5.5 eV),[28-29] amorphous carbon materials have a varied number of carbon rings with short-range ordered nano-graphitic structure and various sp^2/sp^3 ratios, exhibiting a moderate band gap (0.8–5.0 eV).[30] To date, amorphous carbon materials have been prepared by sputtering, vacuum arc deposition, physical laser deposition, e-beam evaporation, etc.[25, 31-32] As one of the physical vapor deposition processes, sputtering can produce thin amorphous carbon films with easy control of the thickness at large-scale (wafer-scale) and at low temperatures independent of the composition of the bottom substrate.

In this study, amorphous carbon films of different thicknesses (1–10 nm) were deposited by carbon sputtering on HfO_2/Si substrates to replace graphene within large (>5 cm^2) catalytic condensers as shown in **Scheme 1**. The carbon films were further thermally treated (400 °C) to induce ordering of amorphous carbon to more graphitic carbon structure with higher sp^2/sp^3 ratios, which
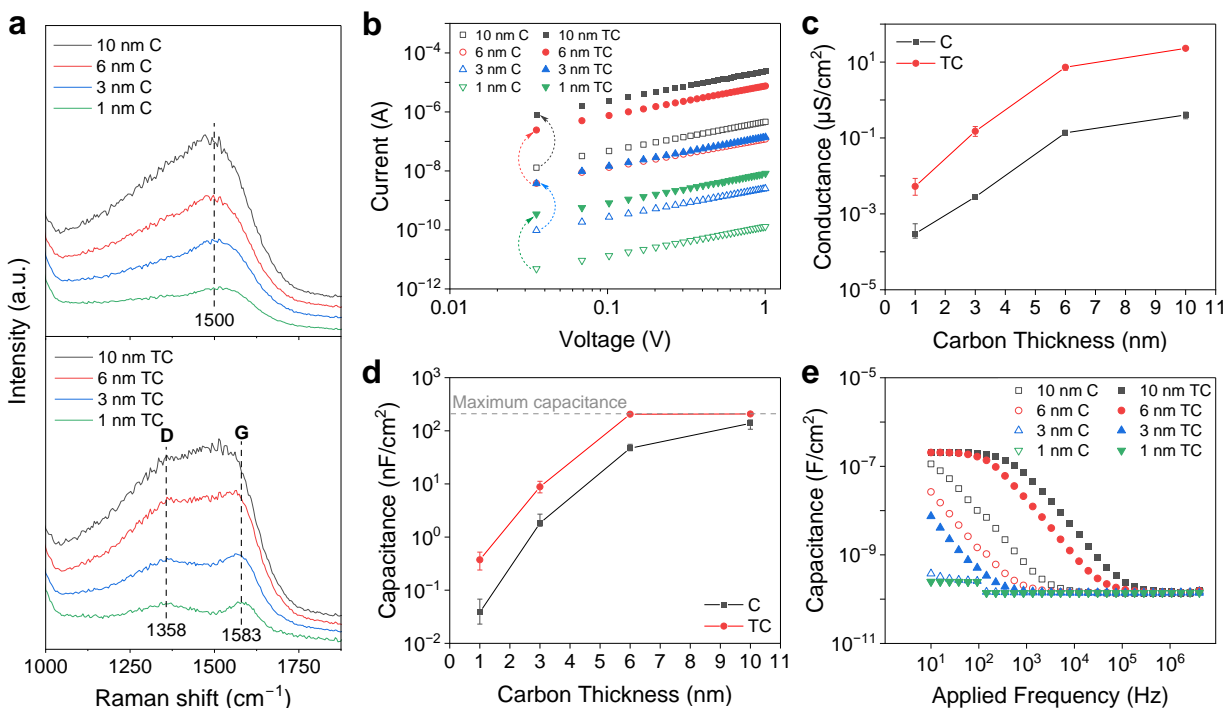
Figure 1. Structural and electronic characterization of carbon (C) and treated carbon (TC) films on HfO$_2$/Si. None of the films contained platinum. **(a)** Raman spectra of the C and TC devices. **(b)** Conductance measured across the 1 cm^2 surface. **(c)** Conductance versus carbon thickness. **(d)** Capacitance of C/HfO$_2$/Si and TC/HfO$_2$/Si stacks versus carbon thickness obtained by I–V curves measured at different sweep rates. **(e)** Capacitance as a function of applied frequency for the same stacks measured by impedance spectroscopy.

increased both the conductance and capacitance. After depositing Pt on top of the carbon films, the resulting Pt-on-carbon device showed high capacitance (~210 nF/cm^2) maintained at applied frequencies up to ~1,000 Hz. More importantly, the temperature programmed desorption experiments with ^{13}CO as a probe molecule showed that the electronic states of the top Pt layer can be modulated by an external voltage bias, indicating that catalytic condensers can function with amorphous carbon films thicker than graphene. Large area Pt-on-carbon devices (8–42 cm^2) were fabricated by the same process, and the linear increment of capacitance with device area with low leakage current/capacitive current ratio (<0.1) was confirmed, indicating that the fabrication of high-quality metal-carbon catalytic condensers is reproducible and functional for programmable catalysis applications.

Results and Discussion. The fabrication process for Pt/C/HfO$_2$/Si catalytic condensers is depicted in **Scheme 1**. As established in our previous studies[13-14], 70 nm of HfO$_2$ as a dielectric material was grown

on a highly conductive p-type Si wafer by atomic layer deposition (ALD) as shown in **Figure S1**. Different thicknesses (1, 3, 6, 10 nm) of carbon film with ~1 cm^2 area were obtained by carbon sputtering on HfO$_2$/Si (C/HfO$_2$/Si) for different durations; carbon films were thermally annealed at 400 °C in air to make thermally treated carbon (TC) devices (TC/HfO$_2$/Si).

To explore the structural properties of C and TC films, C/HfO$_2$/Si and TC/HfO$_2$/Si devices were analyzed by Raman spectroscopy (**Figure 1a**). The C films showed a broad peak centered at ~1500 cm^{-1}, which is generally observed in amorphous carbon materials.[33] After thermal treatment, the Raman spectra of all carbon film thicknesses showed two distinct bands, D and G peaks at 1358 and 1583 cm^{-1}, which originated from the disordered carbon structure and in-plane stretching vibration of sp^2 carbons, respectively.[34] This indicates that the thermal treatment induced re-ordering of amorphous carbon films to form semi-graphitic carbon films. The same result was obtained when the C/HfO$_2$/Si was heated under N$_2$
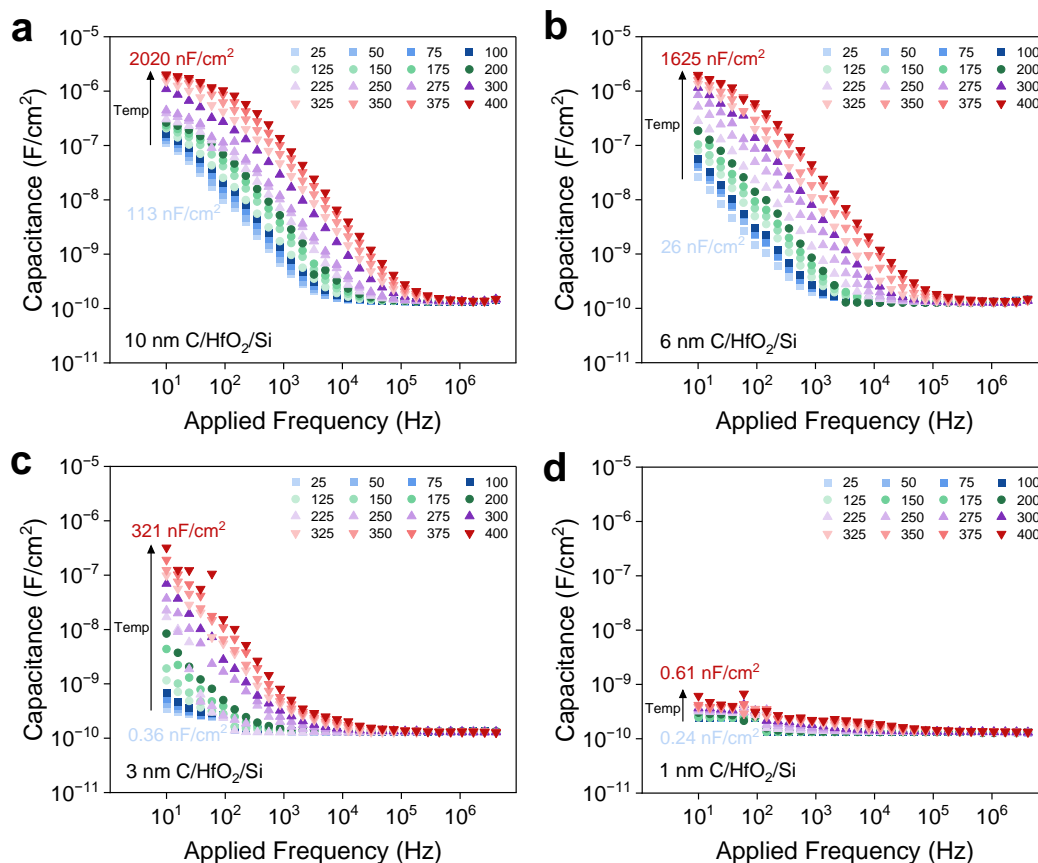
Figure 2. Capacitance of C/HfO₂/Si devices as a function of applied frequency measured by impedance spectroscopy at different temperatures and sputtered carbon film thickness: **(a)** 10 nm C/HfO₂/Si, **(b)** 6 nm C/HfO₂/Si, **(c)** 3 nm C/HfO₂/Si, **(d)** 1 nm C/HfO₂/Si. The insets indicate the temperature (°C) for measurement.

flow, indicating that the re-ordering process occurred by thermal heating (**Figure S2**).

The electronic properties of C/HfO₂/Si and TC/HfO₂/Si devices were characterized for variation in film thickness and thermal treatment by the device setup shown in **Figure S3**. **Figure 1b** shows the conductance of C and TC films measured across the 1.0 cm² top surface of the device plotted in log scale (linear scale results are shown in **Figure S4**). The comparison of carbon film conductance versus thickness of C and TC is summarized in **Figure 1c** and **Table S1**, indicating that the conductance exponentially increased with carbon film thickness. Furthermore, the thermal treatment process enhanced the conductance of carbon films by about an order of magnitude. The amount of accumulated charge in the top layer of a device was determined from the current density–voltage (*I–V*) curves measured from −1 V to 1 V at different sweep rates, from which capacitance was calculated (**Figure S5** and **Figure S6**, see the Supporting

Information for details). The maximum capacitance of metal/HfO₂/Si device was measured to be 207 nF/cm² by depositing Au/Ti (45/5 nm) on HfO₂/Si by e-beam evaporation (**Figure S5**), and the corresponding dielectric constant (*k*) of 70 nm HfO₂ was 16.7.

Figure 1d summarizes the capacitance of the C/HfO₂/Si and TC/HfO₂/Si devices determined from *I–V* curves (**Figure S7–S10**). The capacitance of carbon films significantly increased with film thickness and after the thermal treatment process. The 1 & 3 nm C films have low capacitance (0.068 nF/cm² and 1.2 nF/cm²), while the 6 & 10 nm C films have high capacitance (45 nF/cm² and 143 nF/cm²). After thermal treatment, 6 nm TC and 10 nm TC are able to store most of the charges stabilized by 70 nm HfO₂ dielectric, reaching the maximum capacitance of 206 nF/cm² and 208 nF/cm². It is worth noting that the amorphous HfO₂ did not crystallize after thermal treatment process (**Figure S11**), thus preserving its high dielectric

Oh, et al.

Page 4

constant. This is evidenced by the high capacitance observed in 6 & 10 nm TC/HfO$_2$/Si devices, similar to that of the Au-Ti/HfO$_2$/Si device. In our previous study, the crystallization of HfO$_2$ led to reduction in the dielectric constant. In contrast, the 1 & 3 nm TC films still exhibited low capacitance (0.36 nF/cm^2 and 6.8 nF/cm^2) following thermal treatment.

Figure 1e depicts the capacitance of the carbon films as a function of applied frequency (i.e., dynamic conditions) measured by impedance spectroscopy from 10 Hz to 10 MHz with a 2 V amplitude sinusoidal potential. The capacitance measured at 10 Hz is comparable with the capacitance measured by *I–V* measurements, consistently showing that capacitance at varied frequencies increased with carbon thickness and thermal treatment. The 6 & 10 nm TC/HfO$_2$/Si maintained high capacitance (~210 nF/cm^2) up to ~100 Hz. However, the devices with thinner carbon films showed negligible capacitance or immediate loss of capacitance with increasing frequency indicating that the charge response to the applied frequency is slow due to both low conductance and low capacitance of the thin carbon films.

Amorphous carbon consists of four-fold coordinated sp^3 carbons with no free electrons and three-fold coordinated sp^2 carbons with π–π^* bonding with one free electron. The conduction in the amorphous carbon predominantly originates from the hopping between nanocrystalline graphitic clusters (sp^2 carbons) rather than the non-crystalline sp^3 carbon rings or branches.[35-36] The higher conductance of TC film than C film can therefore be explained by the reduced distance between graphitic clusters consistent with an increase of their size.[37-38] The measured capacitance of C/HfO$_2$/Si and TC/HfO$_2$/Si devices (except for 6 & 10 nm TC/HfO$_2$/Si) are smaller than the maximum capacitance obtained from 70 nm HfO$_2$ dielectric; the sputtered carbon films must therefore be semiconductive materials having low density of states.[39-40] Therefore, an increase of conductance and capacitance after thermal treatment is ascribed to the more graphitic structure (high sp^2/sp^3 ratio) of TC films relative to the C films as evidenced by Raman spectroscopy observed in **Figure 1a**.

To measure the capacitance of carbon devices at elevated temperatures, the C/HfO$_2$/Si devices were measured by impedance spectroscopy at temperatures from 25 °C to 400 °C as shown in **Figure 2a–2d**. The surface temperature of the device surface was confirmed by FLIR camera (**Figure S12**). Notably, 10 nm C/HfO$_2$/Si and 6 nm C/HfO$_2$/Si exhibited significant increase of capacitance from 143 nF/cm^2 and 45 nF/cm^2 at 25 °C to 2,020 nF/cm^2 and 1,625 nF/cm^2 at 400 °C, respectively. These capacitances corresponded to charge (e$^-$ or h$^+$) densities of ~10^{13} cm^{-2} and ~10^{14} cm^{-2} when +1 V or +5 V of voltage bias was applied. Considering the number of surface-active sites in continuous metal layer is estimated to be ~10^{15} cm^{-2},[14] the obtained result indicates that 1–10% of charge per surface atom can be condensed when the catalytic condenser was operated at 400 °C. This result not only indicates an increase of the dielectric constant of HfO$_2$ with temperature but also demonstrates that 6–10 nm carbon films can store significant charge density at higher temperatures. The 3 nm C/HfO$_2$/Si also showed an increase of capacitance from 0.36 nF/cm^2 to 321 nF/cm^2, but the capacitance of 1 nm C/HfO$_2$/Si increased only slightly (0.24 nF/cm^2 to 0.61 nF/cm^2) due to the limited density of states in the 1 nm C film.

The increase in capacitance of HfO$_2$-based catalytic condensers is consistent with the known electronic properties of HfO$_2$. The dielectric constant of a material is determined by the polarizability of its constituents as expressed by the Clausius-Mossotti relation.[41] The thermal coefficient of capacitance can be derived from this, which describes the changes of capacitance with temperature due to: (i) decreased number of polarizable electrons from the volume expansion, (ii) increased polarizability of a constant number of electrons from the increased volume available, (iii) temperature dependence of electron polarizability, and (iv) increased material inhomogeneities from defects and disorder.[42] Consistent with these factors, the dielectric constant of HfO$_2$ dielectric materials is known to increase with temperature.[14, 43] In deed, the impedance spectroscopy measurements at elevated temperatures revealed that the charge-storing capability of the catalytic condenser under reaction conditions (i.e., elevated temperatures) can be much higher than the capacitance of a device at room temperature.

Platinum Catalytic Condensers. Having confirmed the structural and electronic characteristics of C/HfO$_2$/Si and TC/HfO$_2$/Si devices, Pt as the catalytic material was deposited on top of C/HfO$_2$/Si and TC/HfO$_2$/Si by e-beam evaporation. To explore the structure of the Pt
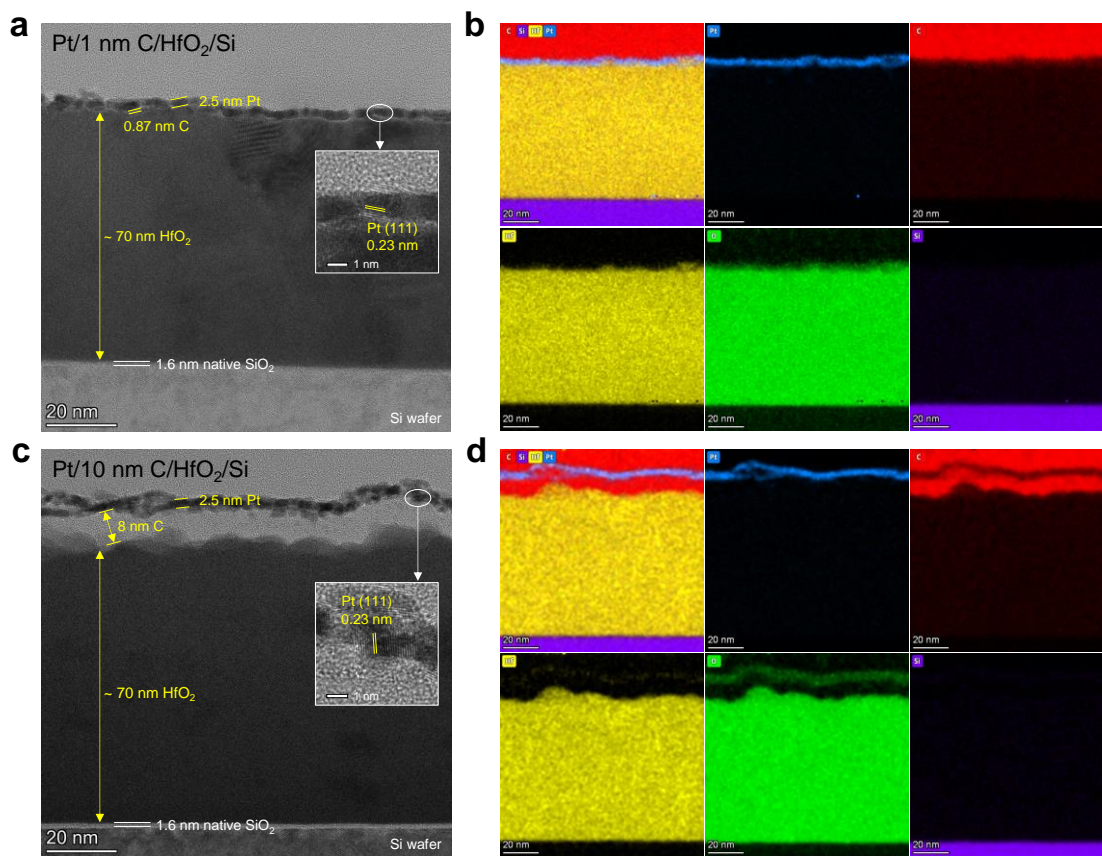
Figure 3. Cross-sectional TEM analysis of Pt/C/HfO$_2$/Si devices. **(a)** TEM image and **(b)** EDS maps of Pt/1 nm C/HfO$_2$/Si. **(c)** TEM image and **(d)** EDS maps of Pt/10 nm C/HfO$_2$/Si. The colors of EDS map indicate Pt (blue), C (red), Hf (yellow), O (green), and Si (purple). The scale bars are 20 nm. The insets in (a) and (c) indicate (111) plane of ~2.5 nm Pt nanoclusters (scale bar = 1 nm).

catalytic condenser, the devices were characterized by transmission electron microscopy (TEM), high-angle annular dark-field scanning TEM (HAADF-STEM) images, and corresponding energy-dispersive X-ray spectroscopy (EDS) analysis, for which cross-sectional devices were prepared by using focused ion beam (FIB). **Figure 3** and **Figure S13–S16** show the TEM images and EDS maps of the Pt/C/HfO$_2$/Si devices with different thickness of carbon films. The device stacks consist of a Si wafer, ~1.6 nm native SiO$_2$, ~70 nm HfO$_2$, 0.8–8 nm carbon film, and Pt nanoclusters in the TEM images. The elements comprising each layer were distinguished by EDS maps. The topmost thick carbon layer is the amorphous carbon protection layer added for preparation of the sample in the FIB process; it is not present in any other experiment. The Pt layer was composed of ~2.5 nm Pt nanoclusters consistent with our previous study,[14] and the (111) planes of Pt (fcc) structure were

observed from these Pt nanoclusters. The surface roughness of HfO$_2$ increased with the carbon thickness due to the high energy of carbon sputtering process, which in turn affected the roughness of the carbon and Pt layers on it.

Based on the *I–V* curves of Pt/C/HfO$_2$/Si and Pt/TC/HfO$_2$/Si devices shown in **Figures S17–S20,** the capacitances of all Pt devices were about the same (195 ~ 210 nF/cm^2), and they matched with the capacitance of Au-Ti/HfO$_2$/Si device (207 nF/cm^2). This result indicates that the top conductive Pt/C or Pt/TC layers store the maximum amount of charge that can be stabilized with the 70 nm HfO$_2$ dielectric film. In addition to the capacitance measured through *I–V* curves, the capacitance relevant to the dynamic conditions necessary for programmable catalysis applications can be determined by measuring capacitance as a function of applied frequency. As shown in **Figure 4a** and **Figure S21**, measurements via impedance
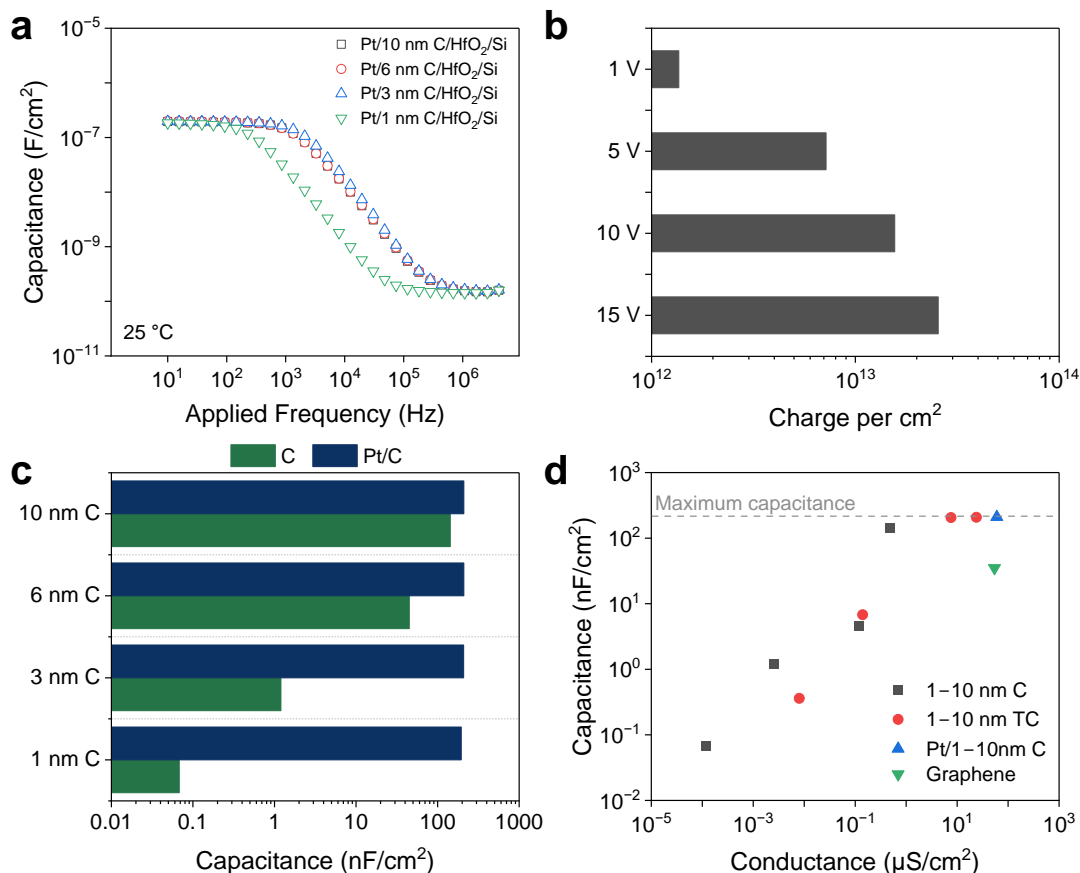
Figure 4. (a) Capacitance of Pt/C/HfO$_2$/Si devices as a function of applied frequency measured by impedance spectroscopy. (b) Charge condensation within Pt/1 nm C/HfO$_2$/Si at varying voltage bias. (c) Comparison of capacitance of C/HfO$_2$/Si and Pt/C/HfO$_2$/Si devices with different carbon thickness. (d) Capacitance versus conductance from catalytic condensers of varying active layer on top of a 70 nm HfO$_2$ layer.

spectroscopy showed that all Pt devices have a capacitance of ~210 nF/cm^2 at 10 Hz. Notably, the capacitance was maintained up to ~1,000 Hz, except for the Pt/1 nm C/HfO$_2$/Si device that showed slightly lower cut-off frequency of ~500 Hz.

The observed increase in conductance and capacitance of condenser devices containing Pt in **Figure 4a** and **Figure S21** indicates the viability of thin amorphous carbon films for programmable catalysis applications. The Pt nanoclusters provide additional states for charge condensation, thereby allowing for Pt/C condenser devices to achieve the maximum capacitance possible with a 70 nm HfO$_2$ film. A benefit of the Pt deposition is increased conductance of the top layer, which then gives rise to a larger cut-off frequency above 1000 Hz for capacitance as seen in **Figure 4a**. Prior reaction simulations have shown that a catalytic condenser switching electronic states at frequencies of 10–

1000 Hz should be sufficiently fast to promote the rate-limiting step (a specific elementary reaction or product desorption), thereby potentially exceeding the Sabatier rate.[5-6, 8]

To explore the capacitance changes of the Pt condenser at high temperatures, a Pt/1 nm C/HfO$_2$/Si device was electronically characterized by impedance spectroscopy at elevated temperatures as shown in **Figure S22**. The result indicated a significant increase of capacitance from 201 nF/cm^2 at 25 °C to 1,544 nF/cm^2 at 400 °C, similar in trend to the carbon C/HfO$_2$/Si devices (**Figure 2**). The capacitance obtained from *I–V* measurement at 400 °C was 1,513 nF/cm^2 similar to the impedance result (**Figure S23**). Considering that 1 nm C/HfO$_2$/Si had negligible capacitance (less than 1 nF/cm^2) at any considered temperature, most of the condensed charges in Pt-containing devices must be in the Pt nanoclusters in the Pt/1 nm C/HfO$_2$/Si. **Figure S24** shows the *I–V* curves of
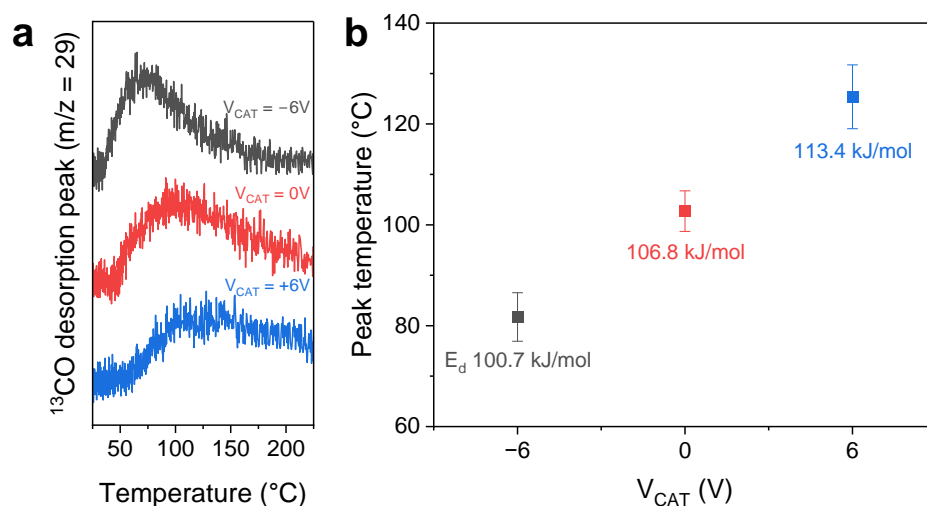
Center for
Programmable
Energy Catalysis

Figure 5. Temperature programmed desorption (TPD) of carbon monoxide. **(a)** ^{13}CO-TPD profiles of Pt/1 nm C/HfO$_2$/Si device with varying potential bias (V$_{CAT}$) of −6 V, 0 V and +6 V. **(b)** The TPD peak maximum temperature of ^{13}CO-TPD varied with V$_{CAT}$; positive potential bias V$_{CAT}$ shifted the TPD peak to higher temperatures, while negative potential bias shifted the TPD peak to lower temperatures. The estimated binding energy of ^{13}CO (E$_d$, kJ/mol) was calculated by the Redhead equation.

Pt/1 nm C/HfO$_2$/Si measured from 0 V to 15 V at different sweep rates (1–2 V/s). Box-shaped *I–V* curves were obtained, indicating that the majority of the current is accumulated in the Pt layer and the Pt/1 nm C/HfO$_2$/Si catalytic condenser has low leakage current even at 15 V. Based on the measured capacitance, the charge areal density (charge per cm^2) was calculated as shown in **Figure 4b**. With 1 V voltage bias, the condensed charge in the Pt layer was about ~10^{12} (e$^−$ or h$^+$) cm$^{−2}$, while ~10^{13} (e$^−$ or h$^+$) cm$^{−2}$ charge amount could be accumulated when 5−10 V was applied, which can effectively modify the electron density of metal sites by ~1% at room temperature. **Figure 4c** compares the measured capacitance of carbon-only (C/HfO$_2$/Si) versus platinum-on-carbon (Pt/C/HfO$_2$/Si) devices. The capacitance of carbon was largely dependent on its thickness, but after Pt deposition, all the devices achieved the maximum capacitance of ~210 nF/cm^2. By this comparison, more charge accumulated in Pt under voltage bias with thinner carbon film layers.

Figure 4d summarizes the capacitance and conductance of several device compositions considered here as well as graphene/HfO$_2$/Si that was used in prior work for comparison.[13-14] The capacitance and conductance were generally proportional on a logarithmic scale, but they also depended on the material characteristics. Amorphous carbon films (6 & 10 nm C) exhibited high conductance (7.6 μS/cm^2 and 23.9 μS/cm^2) that is slightly less than graphene (54 μS/cm^2), but they are not ideal candidate materials for the Pt catalytic condenser due to a large extent of charge condensation within carbon itself. In contrast, although 1 & 3 nm C films exhibited low conductance on their own, they also had negligible capacitance; the result when adding Pt to carbon films (**Figure 4c**) is a highly conductive composite film where most of the condensed charge resides in the Pt nanoclusters.

Temperature Programmed Desorption of ^{13}CO. To evaluate charge modulation of the Pt active layer and examine the Pt/C/HfO$_2$/Si device as a catalytic condenser, the Pt/1 nm C/HfO$_2$/Si device was examined by the method of temperature programmed desorption (TPD) using ^{13}CO as a probe molecule. CO desorption on Pt surface has been intensively investigated such that the binding energy of CO on Pt surface is known to differ by the oxidation state, Pt facets (e.g., (111) vs (100)), and surface coverage.[44-48] It is known that the CO binding energy on the metal surface can be greatly affected by the electronic structure of the metal surface, typically observed from bimetal alloy or metal-support interaction; increasing the electron

density in the metals weakens the bond strength between CO molecule and metal atom, which results in lowered CO desorption temperature. Alternatively, depleting electrons in Pt nanoclusters via positive applied bias ($V_{CAT} > 0$) strengthens the binding energy of ^{13}CO to the surface.

After inserting the catalytic condenser device into a TPD reactor chamber with electronic connections, the system was sealed and preheated at 400 °C in a vacuum to remove any adsorbed molecules on the surface and reactor walls; thereafter the system and device were cooled to room temperature followed by dosing of ^{13}CO to saturate the Pt surface. The reactor was then heated from 20 °C to 400 °C via a linear ramp of 10 K min^{-1} to observe the desorption of ^{13}CO by tracking the mass-to-charge (m/z) of 29 with the quadrupole mass spectrometer.

Figure 5a depicts the ^{13}CO-TPD profiles of the Pt/1 nm C/HfO$_2$/Si device at different applied external voltages (V_{CAT}) of 0 V, −6 V, and +6 V. The results showed that the maximum peak temperature for ^{13}CO desorption from the Pt surface varied with the applied V_{CAT}. Without an external applied voltage (0 V), the measured ^{13}CO desorption peak temperature was 102.4 °C. When negative bias potential was applied ($V_{CAT} = -6$ V), the peak temperature decreased to 78.9 °C due to the accumulation of additional electrons on the exposed Pt layers. In contrast, the peak temperature increased to 112.7 °C when a positive potential bias was applied ($V_{CAT} = +6$ V), due to the depletion of electrons in the Pt layer. From the obtained peak desorption temperatures, the estimated desorption activation energy of ^{13}CO was calculated by the Redhead equation as shown in **Figure 5b** (assuming 1st order kinetics and pre-exponential factor of 10^{13} s^{-1}, see the Supporting Information for details).[49] The ^{13}CO desorption binding energies were 99.8 kJ/mol, 106.7 kJ/mol, and 114.5 kJ/mol when V_{CAT} was −6 V, 0 V, and +6 V. These results are consistent with our previous results evaluating ^{13}CO desorption from a Pt/graphene/HfO$_2$/Si catalytic condenser, although the extent of shifts in the peak temperature and the corresponding desorption activation energies of ^{13}CO were slightly less in this study due to the smaller capacitance of Pt/C/HfO$_2$/Si (210 nF/cm^2) than the previously made Pt/graphene/HfO$_2$/Si (350 nF/cm^2).[14] The observation of a shift in ^{13}CO binding energy indicates that the amorphous-carbon catalytic

condensers have comparable capability for controlling surface chemistry as the earlier graphene-based devices.

Large Area Device Fabrication. Large area Pt/1 nm C/HfO$_2$/Si devices were next fabricated by taking advantage of the carbon sputtering process. On top of a 4" wafer of HfO$_2$/Si, a large square area was outlined with polyimide tape for carbon sputtering and Pt deposition. The obtained large area devices are shown in a photograph in **Figure 6a** using both HfO$_2$ and SiO$_2$ as the dielectric film. These devices exhibited purple and blue colors, respectively. **Figure 6b** and **Figure S25** show the *I–V* curves (y-axis is not normalized to the area) of different-sized Pt/1 nm C/HfO$_2$/Si devices at different sweep rates; all devices featured box-shaped curves, indicating low leakage current even for large area devices. The capacitance of each device was then calculated, and the result was an expected linear increase of capacitance as the area of devices increased as shown in **Figure 6c**. The 8, 21, 29, and 42 cm^2 Pt/1 nm C/HfO$_2$/Si devices exhibited high capacitance of 1,822, 4,421, 6,497, and 9,393 nF, and these values corresponded to ~210 nF/cm^2 after area normalization. This indicated that the large area fabricated device had the same electronic characteristics as the smaller ~1 cm^2 device.

The same large-area fabrication procedures were also performed on different sizes (1, 14, 28 and 46 cm^2) of 100 nm SiO$_2$/Si substrate to produce Pt/1 nm C/SiO$_2$/Si devices. These also showed box shaped *I–V* curves (**Figure S26**) and a linear increase of capacitance with the device size as shown in **Figure 6c**. The ability to switch between dielectric films indicates the versatile utility of carbon sputtering-based large area catalytic condenser fabrication process and the uniformity of the deposited Pt nanoclusters and carbon films on the entire wafer area.

The measured current of a catalytic condenser can be divided into current that passes through the HfO$_2$ insulator (leakage current) and current that accumulates charge in the top Pt/C layer (capacitive current). From the *I–V* curves (**Figure 6b** and **Figure S25**), the relative ratio of the leakage current to the capacitive current at each sweep rate was calculated as shown in **Figure 6d**. All devices exhibited low leakage current/capacitive current values less than 0.1 at every sweep rate, demonstrating that the majority of the current is
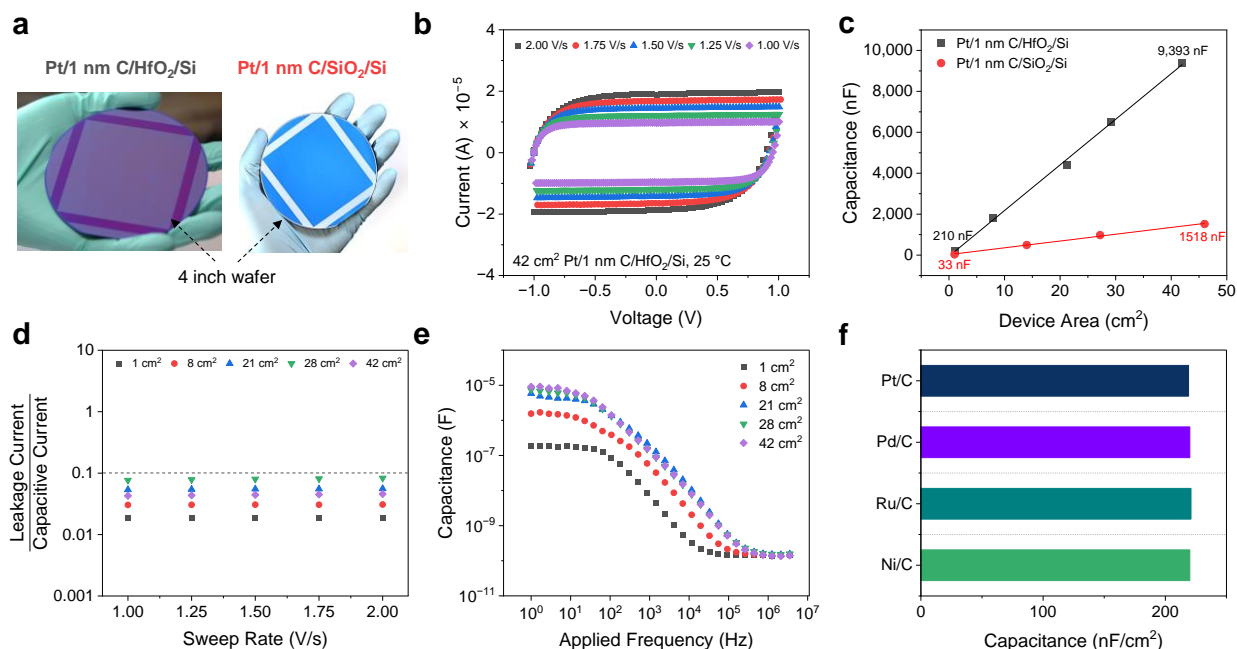
Oh, et al.

Figure 6. Large area catalytic condensers. **(a)** Photograph of 42 cm² Pt/1 nm C/HfO₂/Si and 46 cm² Pt/1 nm C/SiO₂/Si catalytic condensers. **(b)** *I–V* curves of 42 cm² Pt/1 nm C/HfO₂/Si catalytic condenser measured from −1 V to 1 V at different sweep rates. **(c)** Capacitance of Pt/1 nm C/HfO₂/Si and Pt/1 nm C/SiO₂/Si devices with different sizes obtained by *I–V* curves measured at different sweep rates. **(d)** Leakage current/capacitive current ratio of Pt/1 nm C/HfO₂/Si device with different sizes at different sweep rates obtained at 1 V. **(e)** Capacitance of Pt/1 nm C/HfO₂/Si devices with different sizes as a function of applied frequency measured by impedance spectroscopy. **(f)** Capacitance of various metal (Pt, Pd, Ru, Ni)/C/HfO₂/Si catalytic condensers.

accumulated in the Pt layer rather than passing through HfO₂ insulator even for large devices.

The capacitance of the different sized condensers was measured via impedance spectroscopy as a function of frequency as shown in **Figure 6e**. The obtained capacitances of devices at 1 Hz agree with the capacitances obtained from *I–V* measurements (**Figure 6b** and **Figure S25**), but the large area devices exhibited a gradual reduction of capacitance at higher frequencies. This can be attributed to the resistance of the Pt/C layer across the large area of a device; the smaller area devices (1 cm²) exhibited the highest corner frequency consistent with current traveling the shortest distance.

Application of Metal-Carbon Catalytic Condenser. The wafer-scale fabrication method of catalytic condensers by successive ALD (HfO₂ growth), carbon sputtering, and e-beam evaporation (Pt deposition) processes developed in this study provides benefits for future industrial application including time-efficiency, reduced cost, reproducibility, uniformity, and scalability. Securing high capacitance (210 nF/cm²) at ~1000

Hz frequency and low leakage current/capacitive current ratio (< 0.1) even for large-area (42 cm²) devices demonstrated that the metal-carbon catalytic condenser emerges as a new platform device for dynamic catalysis, replacing the previously developed graphene-catalytic condenser, which required high cost, significant time, and effort for device fabrication. The large-area catalytic condenser enables the exploration of catalytic activity as a function of device area, or the amount of catalyst, while modifying their electronic states via steady-state or oscillating applied potential.

The accessibility of other catalytically active metal sources from physical vapor deposition methods such as e-beam evaporation, thermal evaporation, or sputtering, allows facile fabrication of diverse metal-on-carbon catalytic condensers. In addition to Pt/C/HfO₂/Si device, devices of Pd/C, Ru/C, and Ni/C on top of HfO₂/Si were fabricated. As shown in **Figure 6f** and **Figure S27**, the capacitances of each metal/C/HfO₂/Si device were identical to that of Pt/C/HfO₂/Si. These metal-on-carbon catalytic condensers can be utilized

individually or can be combined as a multi-metal catalytic condenser. Another potential technology opportunity would be fabrication of a metallic alloy catalytic condenser (e.g., AuPd/C), which can be produced by depositing alloy sources or by depositing multiple thin metal layers, followed by a heat treatment (reduction) process for the formation of desired metallic alloy phase with exposed different (or more) metal sites. In future work, we aim to show that these advanced metal-on-carbon catalytic condensers can be utilized by applying different voltage bias or oscillation frequency to each metal surface to control the adsorption and desorption behavior of complicated catalytic reactions more precisely, by reducing catalyst poisoning, or by controlling product selectivity.

Experimental Methods. The metal/carbon catalytic condensers were fabricated and characterized as below. The details of fabrication procedure and characterization are described in the Supporting Information.

Metal/carbon Catalytic Condenser Fabrication. The metal/carbon catalytic condensers are fabricated by growing HfO_2 on a conductive p-type Si+++ substrate, followed by carbon sputtering, and metal deposition. 70 nm of HfO_2 film was grown by 500 cycles of ALD process at 100 °C using tetrakis(dimethylamido)hafnium (IV) and water as the HfO_2 and oxygen precursor. Different thickness of carbon film was deposited using a sputter coater (Leica EM ACE600) for 1 cm^2 device. Carbon thread as the carbon source was pulsed at 140 W under vacuum (5.0×10^{-5} torr) until the set thickness (1 nm, 3 nm, 6 nm, 10 nm) of carbon films were achieved by quartz crystal microbalance in the sputtering machine. For large-scale fabrication, graphitic carbon target (99.999%) was used as the carbon source, and the sputtering was conducted with DC sputtering machine (AJA ATC 2000) at 250 W under vacuum (5.0×10^{-6} torr) for 300 seconds. Pt layer was grown on the carbon films by e-beam evaporation (CHA evaporator) by using Pt target source. The detailed device fabrication process is available in the Supporting Information.

Spectroscopy. Raman spectra were obtained from a Witec Alpha 300R confocal Raman microscope equipped with a UHTS300 spectrometer and a DV401 CCD detector. The spectra collection was carried out with an excitation

laser wavelength of 532 nm, grating of 600 g/mm at 40× lens (laser spot size of 0.5 μm in the x–y directions and 1 um in the z direction). The integration time was 5 s and each spectrum was obtained via 10 accumulations. XRD patterns were recorded on a Bruker D8 Discover 2D diffractometer equipped with a Co Kα source (λ = 0.179 nm).

STEM and EDS analyses. The cross-sections of the devices for TEM studies were prepared using focused-ion beam (FEI Helios NanoLab G4 Dual Beam). Approximately 50 nm of protective amorphous carbon was deposited prior to preparation of lamellar cross-sections using a Ga ion beam operated at energies of 30, 5, 2, and 1 keV. HRTEM, STEM, and EDS characterization was performed using a Thermo Fisher Talos F200X G2 microscope equipped with a Super-X EDS spectrometer and Thermo Fisher Velox software. The microscope was operated using an electron beam energy of 200 keV.

Electronic Characterizations. The electronic measurements of the devices were collected by placing the conductive metal probe tips on the surface of the device that connected with a probe station equipped with a source meter (Keithley 2611B and Keithley Test Script Builder). For *I–V* measurements, five different voltage sweep rates (1.00 V/s, 1.25 V/s, 1.50 V/s, 1.75 V/s, 2.00 V/s) were used, and 2.00 V/s sweep rate was used for conductance measurements. The impedance spectra were collected with a Newtons PSM3750 multimeter equipped with an Impedance Analysis Interface 2 from the frequency range from 10 Hz (or 1 Hz) to 10 MHz. For impedance measurements at elevated temperatures, the devices were placed on a conductive metal stage on top of a ceramic hot plate.

Temperature-Programmed Desorption. [13]CO-TPD experiment was performed in a customized ultrahigh vacuum chamber connected with voltage bias-capable setup and a mass spectrometer. The temperature inside the chamber for actual sample temperature (T_{int}) and the exterior temperature (T_{ext}) were different, and a standard temperature calibration curve was made. Prior to each TPD experiment, the chamber preheated at T_{ext} = 400 °C under vacuum, followed by cooling to room temperature. Then, 200 Torr of [13]CO vapor was introduced to the TPD chamber for 10 min for complete saturation on the device's surface, and

then the TPD chamber was evacuated at T_{ext} =100 °C for 1 h to remove any physisorbed ^{13}CO on the device's surface and the chamber wall. After the TPD chamber cooled to room temperature, TPD experiment was conducted by applying a voltage bias (−6 V, 0 V, +6 V) and heating the chamber to T_{ext} = 400 °C at a ramp rate of 10 °C/min. The desorbed ^{13}CO with m/z ratio of 29 was monitored by a quadrupole mass spectrometer during the temperature ramping.

Conclusions. A facile and effective fabrication process was developed for large-area (~42 cm^2) metal-on-carbon catalytic condensers by successive ALD, carbon sputtering, and an e-beam evaporation process. A significant enhancement of conductance and capacitance of carbon films after thermal treatment was observed, which was ascribed to the increase of sp^2/sp^3 ratio by graphitization. Thick carbon (C) and treated carbon (TC) films (6 & 10 nm) had large capacitance, but the capacitance of thin C and TC films (1 & 3 nm) were low, which is desirable for a metal-on-carbon catalytic condensers to enable the condensation of charge predominately in metal clusters. After Pt deposition, the resulting Pt/C/HfO$_2$/Si and Pt/TC/HfO$_2$/Si showed the maximum capacitance (~210 nF/cm^2) independent of the supporting carbon film thickness. Impedance spectroscopy measurements of C/HfO$_2$/Si and Pt/C/HfO$_2$/Si devices at elevated temperatures showed high capacitance (~2,000 nF/cm^2) at 400 °C, demonstrating that the capacitance of catalytic condensers under real reaction conditions (i.e., elevated temperatures) are much higher than the capacitance measured at room temperature. The ^{13}CO-TPD experiments demonstrated shifts of ^{13}CO desorption temperatures when an external potential bias was applied (−6 V and +6 V), which indicates that the electronic state of Pt layer was modulated in a Pt/1 nm C/HfO$_2$/Si catalytic condenser. The large-area Pt/1 nm C/HfO$_2$/Si devices exhibited a linear increase of capacitance as the device area increased, maintaining low leakage current/capacitive current ratio below 0.1. This indicates the uniform distribution of Pt nanoclusters on sputtered carbon films with a high-quality dielectric film within the Pt/C/HfO$_2$/Si stack even in wafer-scale, thereby demonstrating a practical large-area fabrication process for metal/carbon catalytic condenser. The developed method was also applied to a SiO$_2$/Si substrate and different metal sources to further demonstrate the versatility of the application for making metal-carbon catalytic condenser.

Supporting Information. The Supporting Information is available free of charge. Device fabrication, characterization details, electronic measurement details, calculations, and additional references.

References

1. Dumesic, J. A.; Trevino, A. A., Kinetic Simulation of Ammonia Synthesis Catalysis. *J. Catal.* **1989,** *116*, 119-129.
2. Jenks, C.; Lee, H. N.; Lewis, J.; Kagan, C. R.; Nealey, P.; Braun, P.; Holladay, J. E.; Gao, Y.; Sholl, D. S.; Helms, B. A.; Sutherland, J.; Greer, J.; Spadaccini, C. M.; Holm, E.; Rollett, A.; Tway, C. *Basic Research Needs for Transformative Manufacturing*; United States, 2020.
3. Bell, A. T.; Gates, B. C.; Ray, D.; Thompson, M. R. *Basic Research Needs: Catalysis for Energy*; Pacific Northwest National Lab (PNNL): Richland, WA (United States), 2008.
4. Ardagh, M. A.; Abdelrahman, O. A.; Dauenhauer, P. J., Principles of Dynamic Heterogeneous Catalysis: Surface Resonance and Turnover Frequency Response. *ACS Catal.* **2019,** *9* (8), 6929-6937.
5. Ardagh, M. A.; Birol, T.; Zhang, Q.; Abdelrahman, O. A.; Dauenhauer, P. J., Catalytic resonance theory: superVolcanoes, catalytic molecular pumps, and oscillatory steady state. *Catal. Sci. Technol.* **2019,** *9* (18), 5058-5076.
6. Ardagh, M. A.; Shetty, M.; Kuznetsov, A.; Zhang, Q.; Christopher, P.; Vlachos, D. G.;

Abdelrahman, O. A.; Dauenhauer, P. J., Catalytic resonance theory: parallel reaction pathway control. *Chem. Sci.* **2020,** *11* (13), 3501-3510.

7. Gathmann, S. R.; Ardagh, M. A.; Dauenhauer, P. J., Catalytic resonance theory: Negative dynamic surfaces for programmable catalysts. *Chem Catal.* **2022,** *2* (1), 140-163.

8. Shetty, M.; Walton, A.; Gathmann, S. R.; Ardagh, M. A.; Gopeesingh, J.; Resasco, J.; Birol, T.; Zhang, Q.; Tsapatsis, M.; Vlachos, D. G.; Christopher, P.; Frisbie, C. D.; Abdelrahman, O. A.; Dauenhauer, P. J., The Catalytic Mechanics of Dynamic Surfaces: Stimulating Methods for Promoting Catalytic Resonance. *ACS Catal.* **2020,** *10* (21), 12666-12695.

9. Wittreich, G. R.; Liu, S.; Dauenhauer, P. J.; Vlachos, D. G., Catalytic Resonance of Ammonia Synthesis by Dynamic Crystal Strain. *Sci. Adv.* **2022,** *8* (4), eabl6576.

10. Qi, J.; Resasco, J.; Robatjazi, H.; Alvarez, I. B.; Abdelrahman, O. A.; Dauenhauer, P. J.; Christopher, P., Dynamic Control of Elementary Step Energetics via Pulsed Illumination Enhances Photocatalysis on Metal Nanoparticles. *ACS Energy Lett.* **2020,** *5* (11), 3518-3525.

11. Shetty, M.; Ardagh, M. A.; Pang, Y.; Abdelrahman, O. A.; Dauenhauer, P. J., Electric-Field-Assisted Modulation of Surface Thermochemistry. *ACS Catal.* **2020,** *10* (21), 12867-12880.

12. Abdelrahman, O. A.; Dauenhauer, P. J., Energy Flows in Static and Programmable Catalysts. *ACS Energy Lett.* **2023,** *8* (5), 2292-2299.

13. Onn, T. M.; Gathmann, S. R.; Wang, Y.; Patel, R.; Guo, S.; Chen, H.; Soeherman, J. K.; Christopher, P.; Rojas, G.; Mkhoyan, K. A.; Neurock, M.; Abdelrahman, O. A.; Frisbie, C. D.; Dauenhauer, P. J., Alumina Graphene Catalytic Condenser for Programmable Solid Acids. *JACS Au* **2022,** *2* (5), 1123-1133.

14. Onn, T. M.; Gathmann, S. R.; Guo, S.; Solanki, S. P. S.; Walton, A.; Page, B. J.; Rojas, G.; Neurock, M.; Grabow, L. C.; Mkhoyan, K. A.; Abdelrahman, O. A.; Frisbie, C. D.; Dauenhauer, P. J., Platinum Graphene Catalytic Condenser for Millisecond Programmable Metal Surfaces. *J. Am. Chem. Soc.* **2022,** *144* (48), 22113-22127.

15. Ullah, S.; Yang, X.; Ta, H. Q.; Hasan, M.; Bachmatiuk, A.; Tokarska, K.; Trzebicka, B.; Fu, L.; Rummeli, M. H., Graphene transfer methods: A review. *Nano Research* **2021,** *14* (11), 3756-3772.

16. Zhang, Y.; Zhang, L.; Zhou, C., Review of Chemical Vapor Deposition of Graphene and Related Applications. *Acc. Chem. Res.* **2013,** *46* (10), 2329-2339.

17. Levchenko, I.; Ostrikov, K. K.; Zheng, J.; Li, X.; Keidar, M.; Teo, K. B. K., Scalable graphene production: perspectives and challenges of plasma applications. *Nanoscale* **2016,** *8* (20), 10511-10527.

18. Choi, S. H.; Yun, S. J.; Won, Y. S.; Oh, C. S.; Kim, S. M.; Kim, K. K.; Lee, Y. H., Large-scale synthesis of graphene and other 2D materials towards industrialization. *Nat. Commun.* **2022,** *13* (1), 1484.

19. Kumar, R.; Joanni, E.; Singh, R. K.; Singh, D. P.; Moshkalev, S. A., Recent advances in the synthesis and modification of carbon-based 2D materials for application in energy conversion and storage. *Prog. Energy Combust. Sci.* **2018,** *67*, 115-157.

20. Zhu, Y.; Murali, S.; Cai, W.; Li, X.; Suk, J. W.; Potts, J. R.; Ruoff, R. S., Graphene and graphene oxide: synthesis, properties, and applications. *Adv. Mater.* **2010,** *22* (35), 3906-3924.

21. Li, X.; Cai, W.; An, J.; Kim, S. M.; Nah, J.; Yang, D.; Piner, R.; Velamakanni, A.; Jung, I.; Tutuc, E.; Banerjee, S. K.; Colombo, L.; Ruoff, R. S., Large-Area Synthesis of High-Quality and Uniform Graphene Films on Copper Foils. *Science* **2009,** *324* (5932), 1312-1314.

22. Yu, Q.; Lian, J.; Siriponglert, S.; Li, H.; Chen, Y. P.; Pei, S.-S., Graphene segregated on Ni surfaces and transferred to insulators. *Appl. Phys. Lett.* **2008,** *93* (11), 113103.

23. Lee, J.-H.; Lee, E. K.; Joo, W.-J.; Jang, Y.; Kim, B.-S.; Lim, J. Y.; Choi, S.-H.; Ahn, S. J.; Ahn, J. R.; Park, M.-H.; Yang, C.-W.; Choi, B. L.; Hwang, S.-W.; Whang, D., Wafer-Scale Growth of Single-Crystal Monolayer Graphene on Reusable Hydrogen-Terminated Germanium. *Science* **2014,** *344* (6181), 286-289.

24. Mishra, N.; Forti, S.; Fabbri, F.; Martini, L.; McAleese, C.; Conran, B. R.; Whelan, P. R.; Shivayogimath, A.; Jessen, B. S.; Buss, L.; Falta, J.; Aliaj, I.; Roddaro, S.; Flege, J. I.; Boggild, P.; Teo, K. B. K.; Coletti, C., Wafer-

Scale Synthesis of Graphene on Sapphire: Toward Fab-Compatible Graphene. *Small* **2019,** *15* (50), e1904906.

25. Kim, I. S.; Shim, C. E.; Kim, S. W.; Lee, C. S.; Kwon, J.; Byun, K. E.; Jeong, U., Amorphous Carbon Films for Electronic Applications. *Adv. Mater.* **2022,** e2204912.

26. Kang, Y. H.; Lee, S.; Choi, Y.; Seong, W. K.; Han, K. H.; Kim, J. H.; Kim, H. M.; Hong, S.; Lee, S. H.; Ruoff, R. S.; Kim, K. B.; Kim, S. O., Large-Area Uniform 1-nm-Level Amorphous Carbon Layers from 3D Conformal Polymer Brushes. A "Next-Generation" Cu Diffusion Barrier? *Adv. Mater.* **2022,** *34* (15), e2110454.

27. Kakuchi, M.; Hikita, M.; Tamamura, T., Amorphous carbon films as resist masks with high reactive ion etching resistance for nanometer lithography. *Appl. Phys. Lett.* **1986,** *48* (13), 835-837.

28. Wort, C. J. H.; Balmer, R. S., Diamond as an electronic material. *Mater. Today* **2008,** *11* (1-2), 22-28.

29. Schultrich, B., *Tetrahedrally Bonded Amorphous Carbon Films I*. Springer Berlin, Heidelberg: 2018; Vol. 263.

30. Sagar, R. U. R.; Zhang, X.; Xiong, C.; Yu, Y., Semiconducting amorphous carbon thin films for transparent conducting electrodes. *Carbon* **2014,** *76*, 64-70.

31. Rode, A. V.; Luther-Davies, B.; Gamaly, E. G., Ultrafast ablation with high-pulse-rate lasers. Part II: Experiments on laser deposition of amorphous carbon films. *J. Apply. Phys.* **1999,** *85* (8), 4222-4230.

32. Anders, S.; Anders, A.; Brown, I. G.; Wei, B.; Komvopoulos, K.; Ager III, J. W.; Yu, K. M., Effect of vacuum arc deposition parameters on the properties of amorphous carbon thin films. *Surf. Coat. Technol.* **1994,** *68-69*, 388-393.

33. Schwan, J.; Ulrich, S.; Batori, V.; Ehrhardt, H.; Silva, S. R. P., Raman spectroscopy on amorphous carbon films. *J. Appl. Phys.* **1996,** *80* (1), 440-447.

34. Kim, J. H.; Kang, S.; Park, J.-W.; Park, E.-D.; Jun, Y.-K.; Han, J. Y.; Jung, J. H.; Kim, N.; Lee, G.-H., Tailored Hydrogen-Free Carbon Films by Tuning the sp2/sp3 Configuration. *ACS Appl. Electron. Mater.* **2021,** *3* (4), 1771-1779.

35. Dwivedi, N.; Kumar, S.; Malik, H. K.; Govind; Rauthan, C. M. S.; Panwar, O. S., Correlation of sp^3 and sp^2 fraction of carbon with electrical,

optical and nano-mechanical properties of argon-diluted diamond-like carbon films. *Appl. Surf. Sci.* **2011,** *257* (15), 6804-6810.

36. Tian, H.; Ma, Y.; Li, Z.; Cheng, M.; Ning, S.; Han, E.; Xu, M.; Zhang, P. F.; Zhao, K.; Li, R.; Zou, Y.; Liao, P.; Yu, S.; Li, X.; Wang, J.; Liu, S.; Li, Y.; Huang, X.; Yao, Z.; Ding, D.; Guo, J.; Huang, Y.; Lu, J.; Han, Y.; Wang, Z.; Cheng, Z. G.; Liu, J.; Xu, Z.; Liu, K.; Gao, P.; Jiang, Y.; Lin, L.; Zhao, X.; Wang, L.; Bai, X.; Fu, W.; Wang, J. Y.; Li, M.; Lei, T.; Zhang, Y.; Hou, Y.; Pei, J.; Pennycook, S. J.; Wang, E.; Chen, J.; Zhou, W.; Liu, L., Disorder-tuned conductivity in amorphous monolayer carbon. *Nature* **2023,** *615* (7950), 56-61.

37. Dasgupta, D.; Demichelis, F.; Tagliaferro, A., Electrical conductivity of amorphous carbon and amorphous hydrogenated carbon. *Philo. Mag. B* **2006,** *63* (6), 1255-1266.

38. Carey, J. D.; Silva, S. R. P., Disorder, clustering, and localization effects in amorphous carbon. *Phys. Rev. B* **2004,** *70* (23), 235417.

39. Xia, J.; Chen, F.; Li, J.; Tao, N., Measurement of the quantum capacitance of graphene. *Nat. Nanotechnol.* **2009,** *4* (8), 505-509.

40. Dröscher, S.; Roulleau, P.; Molitor, F.; Studerus, P.; Stampfer, C.; Ensslin, K.; Ihn, T., Quantum capacitance and density of states of graphene. *Appl. Phys. Lett.* **2010,** *96* (15), 152104.

41. Rysselberghe, P. V., Remarks concerning the clausius-mossotti law. *J. Phys. Chem.* **1932,** *36* (4), 1152-1155.

42. Cockbain, A. G.; Harrop, P. J., The temperature coefficient of capacitance. *J. Phys. D. Appl. Phys.* **1968,** *1*, 1109-1115.

43. Hu, H.; Zhu, C.; Lu, Y. F.; Li, M. F.; Cho, B. J.; Choi, W. K., A High Performance MIM Capacitor Using HfO_2 Dielectrics. *IEEE Electron. Device Lett.* **2002,** *23* (9), 514-516.

44. Feibelman, P. J.; Hammer, B.; Norskov, J. K.; Wagner, F.; Scheffler, M.; Stumpf, R.; Watwe, R.; Dumesic, J., The CO/Pt(111) Puzzle. *J. Phys. Chem. B* **2001,** *105*, 4018-4025.

45. Ertl, G.; Neumann, M.; Streit, K. M., Chemisorption of CO on the Pt(111) surface. *Surf. Sci.* **1977,** *64*, 393-410.

46. Allian, A. D.; Takanabe, K.; Fujdala, K. L.; Hao, X.; Truex, T. J.; Cai, J.; Buda, C.; Neurock, M.; Iglesia, E., Chemisorption of CO and mechanism of CO oxidation on supported

platinum nanoclusters. *J. Am. Chem. Soc.* **2011,** *133* (12), 4498-4517.

47. Gunasooriya, G. T. K. K.; Saeys, M., CO Adsorption on Pt(111): From Isolated Molecules to Ordered High-Coverage Structures. *ACS Catal.* **2018,** *8* (11), 10225-10233.

48. Gunasooriya, G. T. K. K.; Saeys, M., CO Adsorption Site Preference on Platinum: Charge Is the Essence. *ACS Catal.* **2018,** *8* (5), 3770-3774.

49. Redhead, P. A., Thermal desorption of gases. *Vacuum* **1962,** *12* (4), 203-211.